Focusing of the lowest-order antisymmetric Lamb mode behind a gradient-index acoustic metalens with local resonators

Jinfeng Zhao, Bernard Bonello, Olga Boyko

Focusing of the lowest-order antisymmetric Lamb mode behind a gradient-index acoustic metalens with local resonators

Jinfeng Zhao,[1,2] Bernard Bonello,[2,*] and Olga Boyko[2]

[1]*School of Aerospace Engineering and Applied Mechanics, Tongji University, 100 Zhangwu Road, 200092, Shanghai, China*

[2]*CNRS, UMR 7588, Institut des NanoSciences de Paris, F-75005, Paris, France*

(Received 25 February 2016; revised manuscript received 21 April 2016; published 13 May 2016)

We have investigated the focusing of the lowest-order antisymmetric Lamb mode (A_0) behind a positive gradient-index (GRIN) acoustic metalens consisting of air holes drilled in a silicon plate with silicon pillars erected on one face of the lens. We have analyzed the focusing in the near field as the result of the coupling between the flexural resonant mode of the pillars and the vibration mode of the air/silicon phononic crystal. We highlight the role played by the polarization coherence between the resonant mode and the vibration of the plate. We demonstrate both numerically and experimentally the focusing behind the lens over a spot less than half a wavelength, paving a way for performance of acoustic lenses beyond the diffraction limit. Our findings can be easily extended to other types of elastic wave.

DOI: 10.1103/PhysRevB.93.174306

As a consequence of the exponential decay of evanescent waves in the free space, conventional lenses, either optical or acoustical, do not allow for forming an image containing information finer than half the working wavelength of the light or of the elastic wave. This drawback, known as the "Abbé limit," has long been the foremost barrier to high-resolution imaging, until the early 2000s when Pendry [1] showed that an optical lens with a negative index can restore the evanescent waves issued from the source allowing then for the subdiffraction imaging and for a resolution better than half the wavelength at the focus. From then on, several devices based on this principle, including superlensing photonic crystals [2], optical superlenses [3], hyperlenses [4,5], metalenses [6–9], and Maxwell fish eyes [10,11], have been proposed. These artificial devices either restore the evanescent waves [1–3], or convert them to propagative waves owing to a subwavelength grating inserted in between the object and the objective of a regular optical microscope [4–6]. However, some other devices can focus light into subwavelength spots in the far field owing to the phenomenon of superoscillations and without any contribution from the evanescent waves [12], but they generally lead to low intensity spots. These advances in the focusing of electromagnetic or optical waves found shortly their counterpart in acoustics. Actually, superlensing phononic crystals (PCs) [13–17], acoustic hyperlenses [18], and metalenses [19–22] were proposed almost at the same time. Similarly to the optical lenses listed above, each of these devices was designed to tailor the evanescent waves in order to achieve the subdiffraction focusing of elastic or acoustic waves. It should be noticed however that spots with a size below the diffraction limit have been demonstrated owing to the time dependent illumination of the sample and without any contribution from the evanescent waves [23,24].

The quest for ultimate resolutions has highlighted another type of lens, the gradient-index (GRIN) photonic/phononic crystal. Similar to conventional Wood lenses [25], these optical [26–30] or acoustical [31–36] heterostructures can collimate, make it convergent, or even focalize incident waves owing to their graded effective refractive index or sound velocity along certain directions. These spatial properties result from the gradual variation of either a physical parameter such as the nature of the inclusions [31] or a geometrical parameter such as the filling ratio [32–35]. However, none of the proposed designs has allowed us to overcome the diffraction limit so far [26–36] because of total internal reflection of the waves with high k vectors which hinders the transmission to the background for external focusing. It was further proposed to use metamaterials featuring extraordinary refractive properties instead of photonic crystals [37–41], and the resolution beyond the diffraction limit for visible light was actually demonstrated analytically [37]. However, such a success has not been obtained with elastic waves in solids so far [38–41], nor has it been investigated how large should be the acoustical refractive index (i.e., ratio of the k vector in the lens to the k vector in the background) to attain this objective.

Metamaterials with local resonances generally fulfill this latter requirement since they may display very slow sound velocity, at least near resonances [9,18–21,42–52]. Besides, depending on the shape and dimensions of the resonant inclusions, the resonances may arise at a very low frequency as compared to the Bragg gap, in a region of the reduced Brillouin zone where effective theories apply. This has been demonstrated both theoretically and experimentally, with 2D PCs made of an array of cylindrical pillars regularly erected on a homogeneous thin slab [44–52]. This last structure deserves special attention. Indeed, a single pillar on a plate has compressional and bending resonances that may lead to dynamic effective modulus and mass density both negative when a number of them are gathered to form a metamaterial. Moreover, since the compressional resonant frequency (monopolar) and the bending resonant frequency (dipolar) are mainly sensitive to the height and to the diameter of the pillar, respectively, they can be tuned almost independently from each other. When associated with a GRIN phononic lens on a plate, it may be expected that the bending resonances and the Lamb waves propagating in the plate exhibit polarization coherency, thus allowing for the enhancement of the evanescent waves and in turn for the forming at the focus of a spot containing

*Corresponding author: bernard.bonello@insp.jussieu.fr

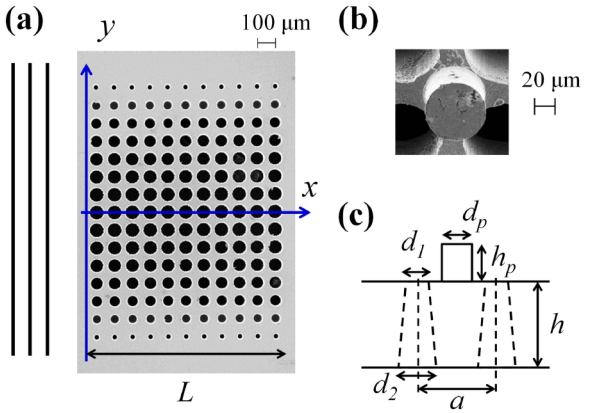

FIG. 1. (a) Scanning electron microscope (SEM) image of the back side of the sample, (b) SEM image of a silicon pillar centered between four air holes on the front side of the sample, and (c) scheme of the sample.

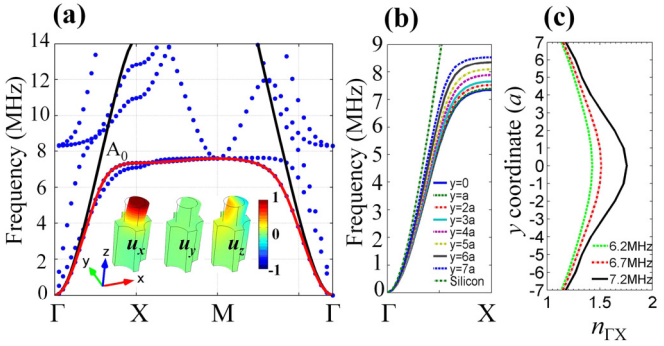

FIG. 2. (a) Band structure (dotted curves) of the trampoline structure along the central layer of the acoustic lens. A_0 band is highlighted by the overlapping red line while the black line indicates the A_0 band along the central layer without pillars. Inset shows the normalized modal displacements of A_0 mode along ΓX at 7.2 MHz. (b) A_0 bands along different horizontal layers of the acoustic lens and the silicon plate. (c) Refraction index profiles along the y axis at several frequencies.

finer information. Based on this idea, we have studied both numerically and experimentally acoustic lenses formed by the association of a GRIN phononic plate with an array of identical pillars. We show in this work that such a structure, sometimes called *trampoline structure* [51], allows for the focalization of an A_0 Lamb mode within the homogeneous substrate behind the metalens, over a spot having a transverse size beyond the diffraction limit. We further describe the underlying mechanism and the role played by the evanescent waves in the formation of the spot.

The acoustic lenses were built on a silicon plate by drilling a square lattice of air holes with radii gradually tailored along the transverse direction (referred hereafter as y axis), as shown by the SEM image in Fig. 1(a). An array of identical silicon pillars was erected on one face of the plate, on each junction between four air holes. The basic unit is shown in Fig. 1(b). The etching technique we used (deep reactive ion etching) led to air inclusions featuring a conical shape with a half top angle of less than 2.5°, as illustrated by the diagram of the unit cell in Fig. 1(c). The holes along the central layer had a diameter of ~90 μm. The period $a = 106\,\mu$m, the thickness of the plate $h = 153\,\mu$m, the diameter of the silicon pillars $d_p = 60\,\mu$m, and their height $h_p = 65\,\mu$m, were all accurately measured with SEM facilities. The x, y, and z axes were parallel to the crystallographic directions of silicon $\langle 100\rangle$, $\langle 010\rangle$, and $\langle 001\rangle$, respectively. We used the values (in GPa) $C_{11} = 165.6$, $C_{12} = 63.9$, $C_{44} = 79.5$ for the elastic constants and $\rho = 2.331$ for the mass density of silicon [32]. In the low frequency region, where the wavelength is much larger than the lattice parameter, the refractive index along each line of inclusions (parallel to the x axis) defined by $n_{\Gamma X} = k_{\Gamma X}/k_B$, i.e., the ratio of the wave number along ΓX to the wave number in the background, was designed to feature a hyperbolic secant profile $n_{\Gamma X}(y) = n_0\,\mathrm{sech}(\alpha y)$, where $\alpha = 0.111$ is the gradient coefficient, and $n_0 = 1.515$ is the refractive index along the central line of inclusions at 6.7 MHz.

The band structure along the central line of the lens where the filling ratio is maximum, computed using the COMSOL finite element method (FEM) package, is shown as dotted lines in Fig. 2(a). In this figure, the antisymmetric Lamb mode A_0 is drawn for a structure with (red solid line) and without (black solid line) pillars. In the inset in Fig. 2(a) are shown the normalized modal displacements associated with A_0 mode at 7.2 MHz for the propagation along ΓX. The corresponding wave number is $k_{\Gamma X} = 0.797\pi/a$. The hybridization between A_0 mode in the air/silicon PC, polarized on the (x-z) plane, and the lowest-order flexural resonance of the pillar is clearly observable. Unambiguously, the pillar's flexural resonance governs the field of displacements, and is responsible for the large down shift of A_0 and the flat branch observed in Fig. 2(a) for the structure with pillars. Therefore, at the resonant frequency the silicon pillars allow for the increase of the wave number and in turn for the significant enlargement of the refractive index. Likewise, the hybridization mode explains the flatness of the A_0 branch around 7.2 MHz since the displacement field is then totally dominated by a vibration localized on the pillars.

The dispersion of A_0 mode along each line of inclusions is displayed in Fig. 2(b). From the external sides of the lens to the central layer, the localized mode arises at a frequency all the more low that the air holes are larger. Accordingly, the index profile was shaped by carefully controlling the radii of the air inclusions. It is worth noting that the geometry of the silicon pillars, and consequently the frequency of the flexural resonance, is perfectly suited to the size of the air holes, as confirmed by the frequencies where the flat branches appear. Actually, the stiffness of the air/silicon PC gets smaller as the filling ratio increases [51], and therefore the frequency of the flexural resonance decreases. This can be easily explained by a basic spring-mass model in which the lowest-order resonant frequency is proportional to the square root of the ratio between the stiffness of the spring and the mass of the resonator. Here a weaker stiffness induced by the lattice of air inclusions gives rise to a smaller flexural resonant frequency.

The profiles along the y axis of the refractive index $n_{\Gamma X}$ at 6.2, 6.7, and 7.2 MHz are drawn in Fig. 2(c). Whatever is the frequency, $n_{\Gamma X}$ takes a value close to 1.2 at the most external layers of the lens and increases to a value along the

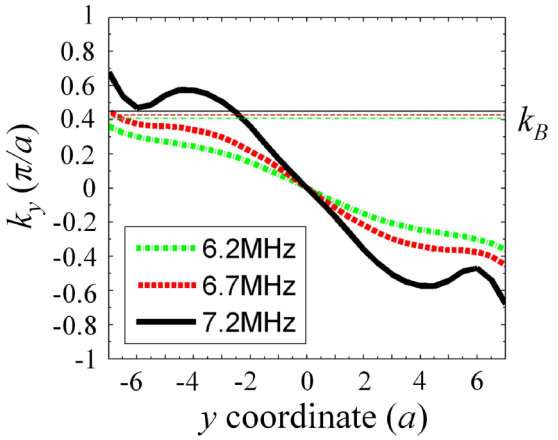

FIG. 3. Transverse wave number k_y along the exit interface against the position of the incident beam along the y axis, together with the corresponding wave number k_B in the background.

central layer all the more larger that the frequency is high. This is consistent with the increasing value taken by the slope of the branch A_0 within the frequency range 6.2–7.2 MHz as y goes from 0 to $7a$ [see Fig. 2(b)]. Assuming that the profile of the refractive index is close to the hyperbolic secant at 6.2 and 6.7 MHz but slightly different at 7.2 MHz, we applied the formalism described in Ref. [53] to calculate the actual shape of the equifrequency contours (EFCs) which may depart from being perfectly circular. We then derived the wave number along each line of inclusions and in turn the ray trajectories within the lens, at any frequency.

Before further analysis, let us mention that by setting the height h_p of the silicon pillars to a value several times that of the lattice constant a, the A_0 band would have been downshifted to the low frequencies region in the Brillouin zone where striking features may be expected [52]. Actually, apart from the difficulty to etch the samples when the pillars feature a large aspect ratio, the coupling of different modes in that case leads to segmented dispersion curves because of intraband gaps and polarization exchanges, and therefore to a much more complex landscape [44,52]. This is the reason why quite low-rise pillars were implemented for this study, allowing for flat continuous bands in the dispersion curves [Fig. 2(a)]. The choice of the value h_p resulted from a compromise leading both to well-marked local resonances and to the absence in the Brillouin zone of the aforementioned drawbacks.

We calculated the ray trajectories within the actual lenses of normally incident elastic waves at 6.2, 6.7, and 7.2 MHz. The length and the width were $L = 11a$ along the x axis and $2D = 14a$ along the y axis, respectively. For all three frequencies, the elastic beam gets focalized within the homogeneous zone behind the lens.

In the long wavelength limit, the value at $x = 0$ of the x-component k_x varies continuously along the y axis according to the hyperbolic secant profile. Beside, as a consequence of Snell's law, k_x keeps a constant value all along the acoustical ray that originates at position $(x = 0, y)$, which translates into $k_x = k_x^0(y)$ [53]. As for the component $k_y(x, y)$, it varies all along the trajectories and takes at the outlet interface between the lens and the background a value that directly affects the size of the spot. We thus have calculated this value against the coordinate along the y axis of the corresponding ray, taken at $x = 0$, for all three frequencies. The results, together with the wave number k_B in the background, are shown in Fig. 3. It should be noted that k_B was set to the maximum modulus of the EFCs which slightly departs from being a circle for A_0 mode in a silicon plate.

At 6.2 and 6.7 MHz the component $|k_y|$ is always less than k_B, and therefore no evanescence arises while the elastic beam at either of these frequencies is transmitted to the background with a real k vector. In contrast, at 7.2 MHz $|k_y|$ is larger than k_B for incident waves falling in the interval $2.5a < |y| < 7a$, and consequently an evanescent component $k_x = i(k_y^2 - k_B^2)^{1/2}$ arises in the background.

Assuming that both the propagative and the evanescent waves converge to form a focus in the near field at a distance L_0 from the outlet interface, it is straightforward to write the transverse profile at the focus as being [2]

$$|U(x,y)| = \left| \begin{array}{l} \int_{-k_B}^{k_B} \exp\left[ik_y y + i\sqrt{k_B^2 - k_y^2}(x - L - L_0)\right]dk_y \\ +\left(\int_{-k_M}^{-k_B} + \int_{k_B}^{k_M}\right) \exp\left[ik_y y + i\sqrt{k_y^2 - k_B^2}(x - L - L_0)\right]dk_y \end{array} \right|, \qquad k_M > k_B, \tag{1}$$

where $|U(x, y)|$ is the field intensity and k_M is the maximum value of $|k_y|$. At 6.2 and 6.7 MHz, where $k_M < k_B$, the second integral in Eq. (1) vanishes, and one must set $|k_y| < k_M$ in the first integral.

From Eq. (1), a main spot with the width between the first two zeros on the y axis $\Delta = 2\pi/k_M$ can be inferred. When $k_M > k_B$, Δ is smaller than the wavelength in the background $\lambda_B = 2\pi/k_B$ [2]. Furthermore, achieving $\Delta < \lambda_B$ requires that the index profile satisfies certain conditions. Actually, let us consider the GRIN PC with a square lattice and let us ignore the anisotropy along each row of inclusions (this is equivalent to assuming that the EFCs are perfectly circular whatever the filling ratio). Under these assumptions, k_M is maximum when the beams issued from the most lateral sides of the lens at $y = \pm D$ converge to the central axis and reads $k_M = n_0 k_B \sqrt{1 - \mathrm{sech}^2(\alpha D)}$. This in turn implies that the lens must feature both a large central refractive index n_0 and a large argument αD. Fulfilling the condition $k_M > k_B$ requires $n_0\sqrt{1 - \mathrm{sech}^2(\alpha D)} > 1$. This actually happens at 7.2 MHz since $n_0\sqrt{1 - \mathrm{sech}^2(\alpha D)} \approx 1.32$ but not at 6.2 or 6.7 MHz. However, in the explored frequency range k_M is always less than π/a, as can be seen from A_0 branches in Fig. 2(b), and therefore the width Δ is always larger than $2a$: similarly to the negative-index superlensing photonic/phononic crystals [2,13,14], the size of the spot along the y axis is limited by twice the lattice constant $2a$. However, we shall mention here

that the symmetry of the lattice and the anisotropy along the lines of inclusions may influence the maximum value of k_M and thus the size of the spot at the focus.

The contribution of both the propagative and the evanescent components may lead to the unconventional subdiffraction focusing in the low frequency region. To give an experimental evidence, we used a noncontact technique both to excite the quasimonochromatic A_0 Lamb mode and to map the out-of-plane displacements in the near field behind the GRIN lens [54,55]. We used ultrashort light pulses issued from a frequency-doubled Nd:YAG laser ($\lambda = 532$ nm, pulse duration 30 ps, repetition 20 Hz) as a photoelastic source. The light pulses first passed through an amplitude mask that created a pattern of alternatively bright and dark fringes and were then focalized on the silicon plate a few millimeters in front of the acoustic lens. A_0 Lamb pulses with a carrier frequency well centered on 7.2 MHz and an envelope containing more than ten cycles were excited normally to the lens by accurately setting the distance between the optical system and the surface of the sample [14]. We used a stabilized Michelson interferometer with a He-Ne laser ($\lambda = 632.8$ nm) as the source, to record the out-of-plane displacements as a function of both time and position. This noncontact technique allowed us to detect out-of-plane displacements as small as a few picometers at any position behind the lens.

We show in Fig. 4(a) the normalized maximum u_z measured behind the acoustic lens from $y = -4.5a$ to $y = 4.5a$. The displacement field is symmetric on both sides of the central layer at $y = 0$, with the overall maximum just behind the lens at $x = 11.6a$ and slightly off-axis ($y = -0.25a$). In addition, lateral peaks, whose origin is explained below, are measured on both sides of the main spot. For comparison, we show in Fig. 4(b) the normalized maximum u_z computed by FEM

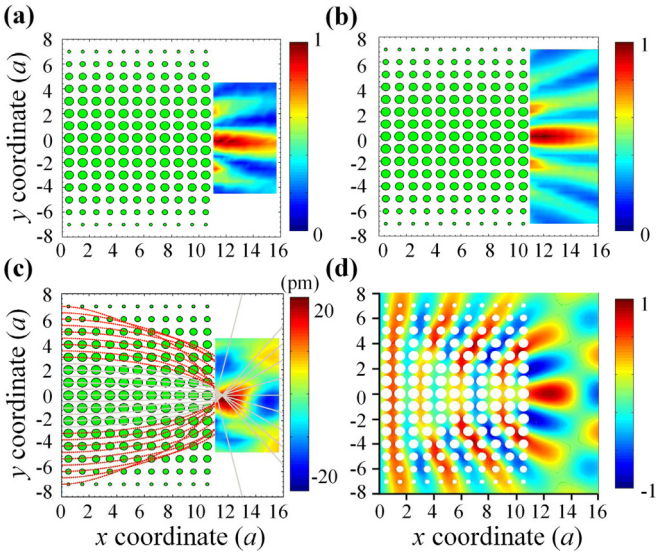

FIG. 4. (a) Experimental and (b) numerical distribution of the normalized maximum u_z behind the acoustic lens at 7.2 MHz, together with (c) experimental and (d) numerical snapshots of the near field focusing at 7.2 MHz. (c) The gray solid lines and the red dashed lines are for the ray trajectories with $|k_y| < |k_B|$ and $|k_y| > |k_B|$, respectively.

where we have implemented an elastic source that perfectly reproduces the experimental conditions, namely an 11-cycled Hanning windowed signal centered on 7.2 MHz. We found the overall maximum centered on the x axis at the position $12.0a$, in good agreement with the experimental results including both the focal position and the pattern of the displacements field. We display also in Figs. 4(c) and 4(d) experimental and numerical snapshots, respectively. The phase patterns in the two snapshots are in good agreement each other.

To further analyze the respective role of the propagative and evanescent waves, the calculated ray trajectories are drawn in Fig. 4(c): the gray solid lines are for the wave with $|k_y| < k_B$ along the exit interface, leading to propagative waves behind the lens, whereas the red dashed lines represent waves with $|k_y| > k_B$, resulting in evanescent waves in the background. The rays corresponding to the propagative waves are converging to a small zone just at the focal position as shown by the experimental results in Figs. 4(a) and 4(c) and the numerical results in Figs. 4(b) and 4(d), giving rise to an overall maximum displacement just behind the lens. At 7.2 MHz, the ratio $k_M/k_B = 1.32$ and according to Eq. (1), it is expected that the evanescent waves allow for a resolution less than half a wavelength at the focus.

We show in Fig. 5 the transverse profile of the normalized maximum u_z, measured experimentally (circular markers), computed using FEM (solid line), or derived from Eq. (1) (dashed line). The experimental data and the simulation or analytical results are in good agreement with each other. Actually, the full width at half maximum (FWHM) of the central peak equates $0.42\lambda_B$, $0.43\lambda_B$, and $0.40\lambda_B$, respectively, with the wavelength in silicon being $\lambda_B = 472.5\,\mu$m at 7.2 MHz. FWHM is less than half a wavelength and the subdiffraction focusing is achieved. However, the analytical results differ from the other two through the lateral peaks which are predicted to be smaller and sharper than it was experimentally and numerically found. This disagreement can be understood by considering Eq. (1) where it is assumed identical contribution of each component k_y at the focus. However, in practice, the elastic waves undergo damping because of internal reflections and impedance losses at the

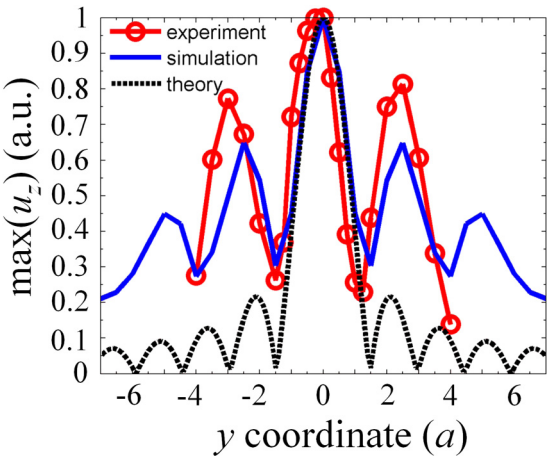

FIG. 5. Experimental (circle markers), numerical (blue solid line), and theoretical (black dashed line) transverse profiles of the normalized maximum u_z at the focus at 7.2 MHz.

interface. As a consequence, the normal displacements are smaller in the central portion of the lens $|y| < 2.5a$ than they are in the edges $2.5a < |y| < D$ [Fig. 4(d)]. In other words the losses are larger when $|k_y| < k_B$ than they are when $|k_y| > k_B$ along the exit interface. Accordingly, both in simulations and in experiments the focus gathers a rate of propagative (evanescent) waves smaller (larger) than predicted by the theory; this leads to a focus along the y axis featuring large side peaks. To accurately calculate the displacement field behind the lens it is therefore necessary to include in Eq. (1) the influence of both the amplitude and the phase of each k vector [2]. However, we can still derive a qualitative conclusion: one needs focalizing the propagative waves to separate the overall maximum value from the truncated interface and one needs gathering the evanescent waves to obtain the subdiffraction resolution at the focus.

To get insights on how the evanescent waves behave along the interface, we have simulated the propagation of the waves through a wedged PC without any gradient, as depicted in Fig. 6. The PC was formed by a square lattice of air holes all having the same diameter such as those located along the layer at $y = \pm 2a$ of the GRIN lens, i.e.,$d_1 = 80\,\mu$m and $d_2 = 85.8\,\mu$m (see Fig. 4), with ΓX orientated along the x axis and all the other parameters unchanged. Just as before, silicon pillars were erected on each corner between four air holes (not drawn in Fig. 6). The PC had a wedged entry interface at an angle of 45° to the x axis. Perfectly matched layers (PML) were introduced in order to mimic the semi-infinite background [48]. A line source was placed in front of the PC to generate incident plane waves with a Gaussian envelope along the transverse direction and the frequency was tuned to 7.2 MHz. The waves were normally incident on the PC with the k vector along ΓM and we checked that no divergence occurred while crossing the interface.

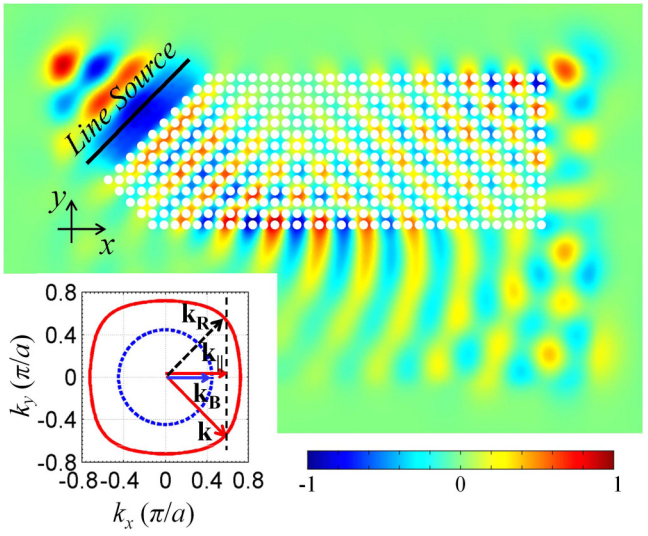

FIG. 6. Simulated propagation of A_0 mode within a wedged phononic crystal plate at 7.2 MHz. Inset: EFCs of both the silicon plate (dashed line) and the PC plate (solid line). Along the exit interface, $\mathbf{k}$ is the incident wave vector, $\mathbf{k}_{//}$ is the component along the interface, and $\mathbf{k_R}$ is the induced wave vector of reflected wave in the PC plate. $\mathbf{k_B}$ is the wave vector in the background.

We show the results in Fig. 6 where evanescent waves with damped amplitude in the silicon background as well as plane waves back-reflected into the PC plate are both clearly observable along the bottom interface. This refraction scheme finds its explanation in the transfer of the wave vector $\mathbf{k}$, as illustrated by the inset in Fig. 6. Along the exit interface, the parallel component $k_{//} = 0.564\,\pi/a$ is larger than k_B as can be seen from the EFCs both in the PC (red solid line) and in the silicon background (blue dashed line), giving rise to the imaginary perpendicular wave number $k_\perp = i \times 0.341\,\pi/a$ and therefore to the damping of the waves in the silicon background. In the first Brillouin zone, the wave vector $\mathbf{k}$ gives also rise to another vector $\mathbf{k_R}$ in the PC plate and therefore to the reflected waves.

At the resonant frequency of the pillars, the coupling with the vibration of the plate leads to a $\mathbf{k}$ vector with a larger module as compared to its value in a GRIN PC without pillar [see Fig. 2(b)]. This obviously affects the refraction of the waves at the interface and the rates of evanescent and reflected waves. Remembering that both the pillars and the plate are made of silicon, they are strongly coupled to each other, giving rise to a moderate quality factor [47,52]. That results in two important consequences: first, while impinging on the interface, the incident elastic energy splits into both evanescent waves and reflected waves. Although the precise proportion of elastic energy on each needs further analysis, it is not expected that one type of wave largely dominates over the other. Second, at resonance the elastic energy gets re-emitted as evanescent waves by the pillars erected close to the interface instead of getting localized in the resonators. A careful examination of Fig. 6 shows that the evanescent waves are guided along the interface, similarly to the "surface-localized modes" observed both in the low frequency region of the Brillouin zone or within the band gaps [56–58]. However, after a few cycles their amplitude decays to a very low level. Actually, the forward traveling evanescent waves always go along with the waves re-emitted by the pillars into the PC plate so that their amplitude decreases. As a result of the conservation of the component $k_{//}$ along the interface, both the re-emitted waves and the reflected waves share the same wave vector $\mathbf{k_R}$, so that re-emission occurs as long as the amplitude of the evanescent waves is not too low. We shall emphasize that the above analysis is based on a single mode approximation and behaviors such as the emission of leaky waves to the silicon plate are ignored here. Moreover, the respective rates of evanescent and reflected waves depend on the frequency since the flexural resonance will change at the same time.

Since $k_{//}$ and $k_\perp$ in Fig. 6 are equivalent respectively to k_y and k_x in Fig. 4, the above description of the evanescent waves along the interface at one given $k_{//} > k_B$ in Fig. 6, can be extended to any wave featuring $|k_y| > k_B$ in Fig. 4: evanescent waves are excited and guided along the interface together with propagative waves reflected to the PC plate. These evanescent waves generated along the exit interface attain the near field focusing on the central layer behind the lens, and thus allow, together with the propagative waves behind the lens, for the focusing with a transverse resolution beyond the diffraction limit, as predicted by Eq. (1).

We show in Fig. 7 the position of the focus along the x axis, together with FWHM (inset) against the frequency, obtained

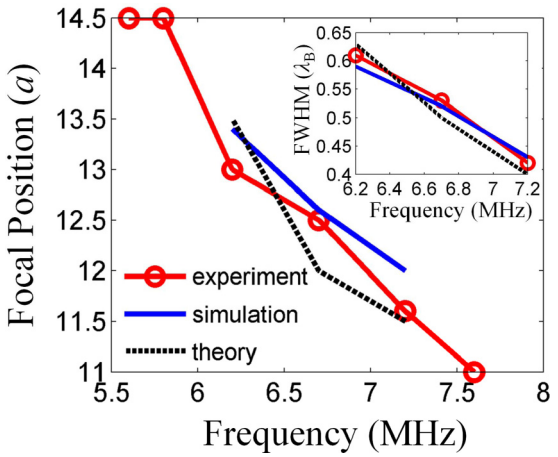

FIG. 7. Experimental (circle markers), numerical (solid line), and theoretical (dashed line) focal position against the frequency, together with the corresponding FWHMs (inset).

experimentally (circular marker), numerically (solid line), and analytically (dashed line). Whatever the method, the results agree well with each other. The position of the focus gets closer to the outlet surface as the frequency increases. This must be ascribed to the variation of the refractive index with frequency as shown in Fig. 2(c). On the other hand, FWHM decreases as the frequency increases, as does the ratio k_M/k_B (see Fig. 3). At 6.7 MHz, k_M/k_B approaches unity and FWHM is just above the diffraction limit (Fig. 7), corresponding to a transitional case from the conventional focusing to the subdiffraction achievement.

In conclusion, we designed a GRIN acoustic metalens comprising a locally resonant uniaxial metamaterial, and we demonstrated both experimentally and numerically the near-field subdiffraction focusing of an A_0 Lamb mode in the MHz range. We analyzed the profile of the transverse component of the **k** vector along the exit interface between the lens and the homogeneous background, and we put into evidence the contributions of both the propagative and the evanescent waves at the focus. Our theoretical analysis, based on a geometrical formalism, applies whatever the type of wave. We further used a laser based experimental technique and a numerical method (FEM) to quantify the size of the spot behind the acoustic metalens: both showed that we obtained a focusing beyond the diffraction limit with the resolution close to 0.43 times the wavelength. These uniaxial metamaterial-based lenses can be implemented at very low frequencies, as well as they can be used to handle the propagation of other types of waves such as the Rayleigh waves. At last, we have investigated the mechanism by which the evanescent waves get localized on the interface and gathered to the focus. The polarization coherence between the flexural resonance of the pillars and the A_0 Lamb mode in the plate enhances the evanescent wave along the interface through the elastic energy re-emitted by the resonators. This enhancement of the evanescent waves through the polarization coherence between the vibration of the resonators and the background medium can be seen as an advantageous strategy to design metalens for other types of waves or to restore the evanescent waves encountered in the negative-index lenses.

[1] J. B. Pendry, Phys. Rev. Lett. **85**, 3966 (2000).
[2] C. Luo, S. G. Johnson, J. D. Joannopoulos, and J. B. Pendry, Phys. Rev. B **68**, 045115 (2003).
[3] N. Fang, H. Lee, C. Sun, and X. Zhang, Science **308**, 534 (2005).
[4] X. Zhang and Z. Liu, Nat. Mater. **7**, 435 (2008).
[5] J. Rho, Z. Ye, Y. Xiong, X. Yin, Z. Liu, H. Choi, G. Bartal, and X. Zhang, Nat. Commun. **1**, 143 (2010).
[6] Z. Liu, S. Durant, H. Lee, Y. Pikus, N. Fang, Y. Xiong, C. Sun, and X. Zhang, Nano Lett. **7**, 403 (2007).
[7] L. Verslegers, P. B. Catrysse, Z. F. Yu, and S. Fan, Phys. Rev. Lett. **103**, 033902 (2009).
[8] F. Lemoult, G. Lerosey, J. de Rosny, and M. Fink, Phys. Rev. Lett. **104**, 203901 (2010).
[9] D. Lu and Z. Liu, Nat. Commun. **3**, 1205 (2012).
[10] Y. G. Ma, S. Sahebdivan, C. K. Ong, T. Tyc, and U. Leonhardt, New J. Phys. **14**, 025001 (2012).
[11] J. C. Miñano, J. Sánchez-Dehesa, J. C. González, P. Benítez, D. Grabovičkić, J. Carbonell, and H. Ahmadpanahi, New J. Phys. **16**, 033015 (2014).
[12] F. M. Huang and N. I. Zheludev, Nano Lett. **9**, 1249 (2009).
[13] A. Sukhovich, B. Merheb, K. Muralidharan, J. O. Vasseur, Y. Pennec, P. A. Deymier, and J. H. Page, Phys. Rev. Lett. **102**, 154301 (2009).
[14] J.-F. Robillard, J. Bucay, P. A. Deymier, A. Shelke, K. Muralidharan, B. Merheb, J. O. Vasseur, A. Sukhovich, and J. H. Page, Phys. Rev. B **83**, 224301 (2011).
[15] X. Zhou and G. Hu, Appl. Phys. Lett. **98**, 263510 (2011).
[16] I. A. Veres, T. Berer, O. Matsuda, and P. Burgholzer, J. Appl. Phys. **112**, 053504 (2012).
[17] H. Jia, M. Lu, Q. Wang, M. Bao, and X. Li, Appl. Phys. Lett. **103**, 103505 (2013).
[18] J. Li, L. Fok, X. Yin, G. Bartal, and X. Zhang, Nat. Mater. **8**, 931 (2009).
[19] J. Zhu, J. Christensen, J. Jung, L. Martin-Moreno, X. Yin, L. Fok, and X. Zhang, Nat. Phys. **7**, 52 (2011).
[20] J. Christensen and F. J. G. de Abajo, Phys. Rev. Lett. **108**, 124301 (2012).
[21] F. Lemoult, N. Kaina, M. Fink, and G. Lerosey, Nat. Phys. **9**, 55 (2013).
[22] T. Brunet, J.-L. Thomas, and R. Marchiano, Phys. Rev. Lett. **105**, 034301, (2010).
[23] M. Dubois, M. Farhat, E. Bossy, S. Enoch, S. Guenneau, and P. Sebbah, Appl. Phys. Lett. **103**, 071915 (2013).
[24] M. Dubois, E. Bossy, S. Enoch, S. Guenneau, G. Lerosey, and P. Sebbah, Phys. Rev. Lett. **114**, 013902 (2015).
[25] C. Gomez-Reino, M.V. Perez, and C. Bao, Gradient-Index Optics in *Fundamentals and Applications* (Springer, Berlin, 2002).
[26] T. Driscoll, D. N. Basov, A. F. Starr, P. M. Rye, S. Nemat-Nasser, D. Schurig, and D. R. Smith, Appl. Phys. Lett. **88**, 081101 (2006).
[27] H. Kurt and D. S. Citrin, Opt. Express **15**, 1240 (2007).
[28] H. Gao, B. Zhang, S. G. Johnson, and G. Barbastathis, Opt. Express **20**, 1617 (2012).

[29] K.-V. Do, X. Le Roux, D. Marris-Morini, L. Vivien, and E. Cassan, Opt. Express **20**, 4776 (2012).
[30] B. Vasić and R. Gajić, J. Appl. Phys. **110**, 053103 (2011).
[31] S.-C. S. Lin, T. J. Huang, J.-H. Sun, and T.-T. Wu, Phys. Rev. B **79**, 094302 (2009).
[32] T.-T. Wu, Y. T. Chen, J.-H. Sun, and T. J. Huang, Appl. Phys. Lett. **98**, 171911 (2011).
[33] J. Zhao, R. Marchal, B. Bonello, and O. Boyko, Appl. Phys. Lett. **101**, 261905 (2012).
[34] T. M. Chang, G. Dupont, S. Enoch, and S. Guenneau, New J. Phys. **14**, 035011 (2012).
[35] Y. Ye, M. Ke, Y. Li, T. Wang, and Z. Liu, J. Appl. Phys. **114**, 154504 (2013).
[36] A. Climente, D. Torrent, and J. Sánchez-Dehesa, Appl. Phys. Lett. **105**, 064101 (2014).
[37] C. Ma, M. A. Escobar, and Z. W. Liu, Phys. Rev. B **84**, 195142 (2011).
[38] L. Zigoneanu, B.-I. Popa, and S. A. Cummer, Phys. Rev. B **84**, 024305 (2011).
[39] Y. Li, B. Liang, X. Tao, X. Zhu, X. Zou, and J. Cheng, Appl. Phys. Lett. **101**, 233508 (2012).
[40] X. Yan, R. Zhu, G. Huang, and F.-G. Yuan, Appl. Phys. Lett. **103**, 121901 (2013).
[41] D. Torrent, Y. Pennec, and B. Djafari-Rouhani, Phys. Rev. B **90**, 104110 (2014).
[42] Z. Liu, X. Zhang, Y. Mao, Y. Y. Zhu, Z. Yang, C. T. Chan, and P. Sheng, Science **289**, 1734 (2000).
[43] S. Yao, X. Zhou, and G. Hu, New J. Phys. **12**, 103025 (2010).
[44] T.-C. Wu, T-.T. Wu, and J.-C. Hsu, Phys. Rev. B **79**, 104306 (2009).
[45] Y. Pennec, B. Djafari-Rouhani, H. Larabi, J. O. Vasseur, and A.-C. Hladky-Hennion, Phys. Rev. B **78**, 104105 (2008).
[46] Y. Pennec, B. Djafari-Rouhani, H. Larabi, A. Akjouj, J. N. Gillet, J. O. Vasseur, and G. Thabet, Phys. Rev. B **80**, 144302 (2009).
[47] R. Zhu, X. N. Liu, G. L. Huang, H. H. Huang, and C. T. Sun, Phys. Rev. B **86**, 144307 (2012).
[48] A. Khelif, Y. Achaoui, S. Benchabane, V. Laude, and B. Aoubiza, Phys. Rev. B **81**, 214303 (2010).
[49] R. Pourabolghasem, S. Mohammadi, A. A. Eftekhar, A. Khelif, and A. Adibi, Appl. Phys. Lett. **105**, 231908 (2014).
[50] M. Oudich, B. Djafari-Rouhani, Y. Pennec, M. B. Assouar, and B. Bonello, J. Appl. Phys. **116**, 184504 (2014).
[51] O. R. Bilal and M. I. Hussein, Appl. Rev. Lett. **103**, 111901 (2013).
[52] M. Rupin, F. Lemoult, G. Lerosey, and P. Roux, Phys. Rev. Lett. **112**, 234301 (2014).
[53] J. Zhao, B. Bonello, R. Marchal, and O. Boyko, New J. Phys. **16**, 063031 (2014).
[54] K. Kokkonen and M. Kaivola, Appl. Rev. Lett. **92**, 063502 (2008).
[55] J. Pierre, O. Boyko, J. O. Vasseur, L. Belliard, and B. Bonello, Appl. Phys. Lett. **97**, 121919 (2010).
[56] B. Manzanares-Martínez and F. Ramos-Mendieta, Phys. Rev. B **68**, 134303 (2003).
[57] D. Zhao, Z. Liu, C. Qiu, Z. He, F. Cai, and M. Ke, Phys. Rev. B **76**, 144301 (2007).
[58] R. Sainidou, B. Djafari-Rouhani, and J. O. Vasseur, Phys. Rev. B **77**, 094304 (2008).